Resolvent analysis of separated and attached flows around an airfoil at transitional Reynolds number

Nikitas Thomareis* and George Papadakis†

Dept. of Aeronautics, Imperial College, London SW7 2AZ, UK

(Dated: June 14, 2018)

Abstract

We analyze the resolvent operator in three flows around a nominal NACA-0012 airfoil at $Re_C = 50,000$ and 5^o angle of attack. In particular, we study two naturally developing flows (around the airfoil with straight and blunt trailing edges) and one tripped flow. The naturally developing flows exhibit laminar separation, transition and turbulent reattachment, while the tripped flow remains attached in the suction side. For all cases, the time-averaged flow fields are computed from separate DNS simulations. The resolvent analysis can identify the areas of maximum receptivity of the flow field as well as the most amplified modes (optimal response). The former was located close to the leading edge, and in the case of naturally developing flows, also in the free-stream. The spatial distribution of optimal forcing was dominated by structures tilted against the mean flow, in agreement with other studies of boundary layer flows. The optimal response of the two naturally developing flows were different. For the NACA-0012 airfoil with straight trailing edge, the response was maximized at the natural frequency of the separating shear layer, and the shape matched closely with the corresponding DMD mode obtained from processing the DNS results. For the blunt airfoil, the receptivity of the separating shear layer was suppressed in the region of natural frequency, while it was maximized at the frequency of vortex shedding from the trailing edge. This is attributed to the lock-in mechanism between the shedding and the separating shear layer observed in the DNS simulations; the lock-in makes the separating shear layer less sensitive to forcing. In the tripped flow, the amplification of the perturbations is significantly diminished, and only by restricting the resolvent analysis to a region close to the suction side can we get a dominant frequency that matches with DNS at that region. The dominant resolvent modes were used to get estimations of the velocity spectra based only on the mean flow and the signal of one velocity component at discrete calibration points. Very good approximation is observed with only one or two points (depending on the flow examined), provided that they are located in energetic regions of the flow that contain sufficient spectral content at the relevant frequencies.

* nikitas.thomareis12@imperial.ac.uk

† g.papadakis@imperial.ac.uk

I. Introduction

The approximation of the solution of the Navier-Stokes equations with a finite number of modes has been a topic of intense research for many decades. Linear stability analysis was one of the earliest attempts to reduce complexity and describe flows with a finite number of modes (see Gaster [1, 2], Schmid and Henningson [3]). Linear stability is an operator-driven technique, i.e. extracts the modes by formulating and solving an eigenvalue problem based directly on the (linearized) Navier Stokes operator. On the other hand, data-driven techniques operate directly on the field data produced from simulations or experiments. Proper orthogonal decomposition (Lumley [4], Sirovich [5]) and the more recent, dynamic mode decomposition (DMD), proposed by Schmid [6] belong to the latter family.

At approximately the same time as DMD, a similar but operator-driven method, based on the resolvent operator was proposed by McKeon and Sharma [7] for the analysis of turbulent flows. The resolvent operator has long been studied in the context of spectral theory of linear operators (refer for example to the book of Kato [8]). This operator maps the input (forcing) applied to a linear system to the output in the frequency domain. In the context of turbulent flows, the resolvent relies on the assumption that the time-average (mean) velocity field is known. The Reynolds decomposition is applied to the Navier-Stokes equations and the transport equations of the perturbation velocities around the mean flow are derived. The non-linear terms are retained (i.e. they are not ignored as in linear stability analysis) and constitute the input (forcing) term. The resolvent operator, based on the time-average velocity, maps this input to the output (perturbation velocities and pressure). More details on the mathematical formulation will be given in section III below. The recent work of Sharma *et al.* [9] provides the mathematical link between the DMD and resolvent modes.

The singular value decomposition (SVD) of the resolvent operator provides the set of turbulent forcings that will yield the largest optimal response on the flow field at a particular frequency. This approach, proposed by McKeon and Sharma [7], has been applied in different contexts and flow configurations. In the original paper [7] it was applied in a turbulent pipe flow and used to study the most energetic modes at a given temporal frequency and wavenumber pair (azimuthal and streamwise). Based on the spatial structure of the modes, the authors identified regions along the radial direction where different scaling laws apply. Similar analysis for a turbulent channel flow was presented in Moarref *et al.* [10].

Beneddine *et al.* [11] employed the resolvent approach to study the conditions for validity of mean flow stability analysis. They concluded that in cases where a strong convective instability is present, and the first singular value of the resolvent operator is several orders of magnitude larger than the rest, then the corresponding resolvent mode will approximate well the spectral mode (i.e. the result of a stability analysis). Thus, in such cases, the spectral analysis of the linearised flow field (around the mean) will indeed yield a good approximation of the actual modes.

The resolvent operator can be also applied for laminar flows. In this context, the optimal response to an externally applied forcing is computed. Sipp *et al.* [12] applied the resolvent operator to capture the Tollmien-Schlichting (TS) waves in a laminar (Blasius) boundary layer. Åkervik *et al.* [13] also studied a flat plate boundary layer flow, and computed optimal forcings and responses using a reduced order model based on global eigenmodes. The same approach was used by Alizard *et al.* [14] for a separated boundary layer in a flat plate. Such an approach suffers from convergence problems and this motivated Sipp and Marquet [15] to compute the singular values directly. Monokroussos *et al.* [16] computed 3D optimal disturbances in a boundary layer flow using a time-stepping algorithm for the forward and adjoint equations. Sartor *et al.* [17] used the resolvent operator to study the shock wave-boundary layer interaction on a OAT15A supercritical airfoil. While the global stability analysis captured the major source of instability (shock buffeting), the modes of the resolvent operator captured secondary pseudo-resonance phenomena, attributed to convective instabilities in the flow field.

When the first singular value is much larger than the rest, the resolvent operator can also be used to derive low order models of the flow. Moarref *et al.* [10] used this feature to successfully approximate the energy density in a turbulent channel flow. The same property can be employed to reconstruct the unsteady dynamics of a flow field using just the mean flow and a signal from one (or more) discrete points. For example Gómez *et al.* [18] used the mean flow and data from a single probe to estimate the three dimensional flow inside a cavity with 5% error. The probe location, and in particular the energy content at the selected location, was found to have an important effect on the quality of estimation. Gómez *et al.* [19] estimated the lift and drag coefficients on a square cylinder using data from a single point in the wake; the results were in very good agreement with DNS data. Beneddine *et al.* [11], used resolvent analysis to estimate the energy spectra of the flow field in a backward

facing step using again a single probe point.

In previous works, the resolvent operator was applied to either laminar (attached or separated) or fully turbulent flows (pipe, channel, jet, backward facing step etc). Most flows were also homogenous in two directions (or weakly inhomogeneous in one direction). In the current work, we apply the resolvent analysis to three highly inhomogenous flows around a nominal NACA-0012 airfoil. All flows contain two dynamically important and interacting regions; the suction side and the wake of the airfoil. Two of the flows were studied recently by the authors using DNS [20]; both are separating and reattaching flows in the transitional regime. The ability of the resolvent operator to reproduce the spectra is also explored in such highly complex flow conditions. New simulations were also performed for a third, tripped, flow. In the latter case, the flow quickly transitions to turbulence and remains attached in the suction side.

The paper is organised as follows. In section II the flows are briefly described and the computational details are provided for the third flow case. The mathematical formulation of the resolvent operator is provided in section III. Results from the resolvent analysis are presented in section IV, while section V explores the estimation of velocity spectra using information from discrete points. Finally, section VI summarises the main findings of this work.

II. Description of the flows examined and computational details

Three flows are considered in the paper; two naturally developing flows (around a NACA-0012 airfoil with straight and blunt trailing edges) and one tripped flow around the standard airfoil. The blunt trailing edge was formed by truncating the rear part at a distance $h = 0.133c$ from the trailing edge, thus exposing a uniform bluntness of thickness $\epsilon = 0.037c$. In all cases, the Reynolds number based on the nominal chord was $Re_c = 50,000$, while the airfoils were placed at 5^o angle of attack. In the following, frequencies are normalised with the nominal chord, c, and the velocity at infinity, U_∞.

The two naturally developing flows are the same as the ones considered by Thomareis and Papadakis [20]; mesh resolution and code validation studies are presented in the same paper. For both flows examined, there is laminar separation, transition to turbulence and turbulent reattachment of the shear layer in the suction side of the airfoil. For the straight

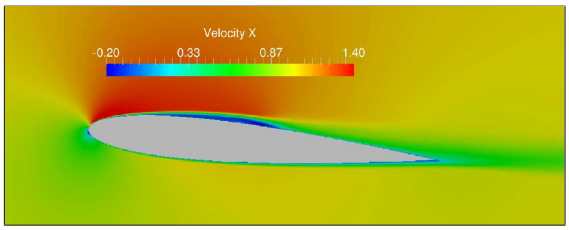

(a) Naturally developing flow - Straight TE.

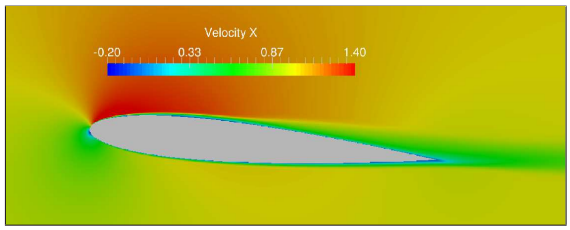

(b) Tripped flow - Straight TE.

FIG. 1: Mean streamwise velocity field for the naturally developing and tripped flows around the straight trailing edge airfoil.

trailing edge airfoil, the flow separates at $x/c = 0.145$, starts to transition at around 0.45 and reattaches at 0.56. Figure 1a presents the mean streamwise velocity. The dynamics of the suction side is dominated by the fundamental and subharmonic of the Kelvin-Helmholtz instability that develops naturally in the separating shear layer (with frequencies 7.4 and 3.8 respectively).

The blunt trailing edge results in periodic vortex shedding with frequency 4.5, which is close to the subharmonic of the natural shear layer frequency. The shedding forces the separating shear layer, and due to this forcing, the shear layer frequency locks onto the shedding frequency while the natural frequency and its subharmonic are suppressed. The time average flow is shown in figure 2. The flow in the suction side is qualitatively similar compared to the straight trailing edge airfoil shown in 1a. There are some differences in the separation and reattachment points (refer to [20] for details). The most important difference is the presence of a small recirculation zone in the near wake due to the presence of bluntness.

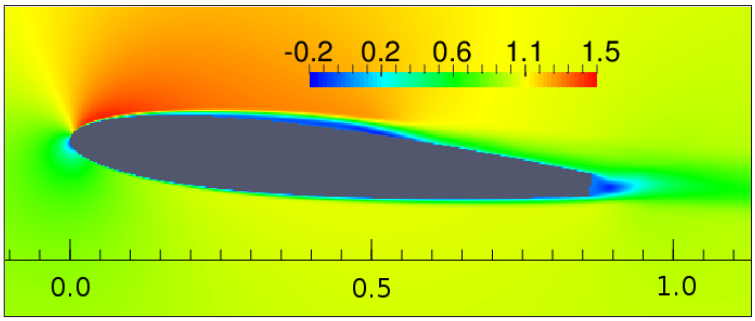

FIG. 2: Mean streamwise velocity field for the naturally developing flow around the blunt trailing edge airfoil.

New DNS simulations were performed to collect data for the tripped flow. The same in-house code, PantaRhei, was used. It is based on the finite volume method and uses a second

order central scheme for the spatial discretisation of the convection and diffusion terms, as well as a second order backwards scheme for time advancement. It is parallelised with the aid of the PETSc library [21]. An algebraic multigrid preconditioner from the Hypre library [22] is used to accelerate the solution of the pressure correction equation.

For the tripped flow simulations, the same mesh was used as for the naturally developing flow. To implement tripping, a slightly modified version of the forcing method of Schlatter and Örlü [23] was employed. More specifically, the original method applies a weak random volume forcing in the wall normal direction, which enters as a source term in the Navier-Stokes equations. In the present version, we compute a random velocity which serves as a wall boundary condition in the spanwise direction. This is applied in a thin strip located shortly downstream of the leading edge, at $x/c = 0.04 - 0.06$. This is an area of maximum sensitivity (as shown in section IV A), thus, any perturbation introduced there is expected to have a large impact on the flow. The spanwise wall velocity is computed from

$$w(z,t) = AU_\infty \left([1 - b(t)]\, h(z)^i + b(t) h(z)^{i+1} \right) \tag{1}$$

where A is the user-defined amplitude of the forcing and $h(z)$ is a randomly generated harmonic function. The value of A was chosen to be 0.05 (i.e. the tripping velocity has a maximum value of 5% of the free stream velocity). Function $h(z)^i$ is a random harmonic mode with unit amplitude for wavenumbers smaller than $2\pi/z_s$ (z_s is 4 times the grid size in the spanwise direction). The following auxiliary functions are used, $b(t) = 3p(t)^2 - 2p(t)^3$, where $p(t) = \frac{t}{t_s} - i$ and $i = int\left(\frac{t}{t_s}\right)$ where t_s defines the time scale of forcing and int denotes the integer part of the division. In the present work, t_s was chosen to be $5\delta t$, where δt is the simulation time step.

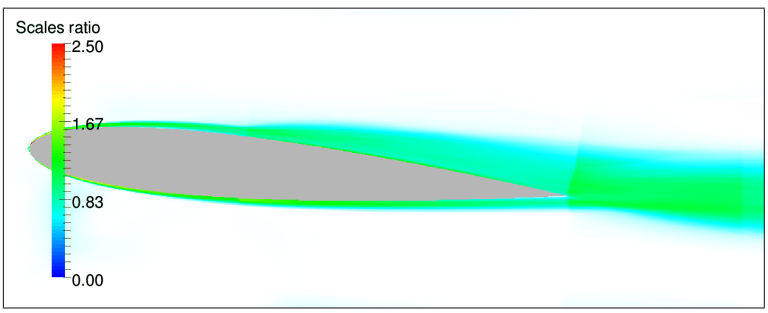

FIG. 3: Ratio of the local characteristic cell size to the Kolmogorov length scale.

Unlike the naturally developing flow around a NACA-0012 at the examined Reynolds number and angle of attack, for the tripped flow there are no reference experimental or numerical data to serve as validation. To check the grid resolution, we compare a characteristic length scale of the mesh (cubic root of the cell volume) with the Kolmogorov length scale $\eta = \left(\frac{\nu^3}{\epsilon}\right)^{1/4}$, where ν is the kinematic viscosity and $\epsilon = \nu\left\langle \frac{\partial u_i}{\partial x_j}\frac{\partial u_i}{\partial x_j} \right\rangle$ is the local dissipation rate. Contours of the ratio between the grid and dissipation length scales are plotted in Figure 3. It can be seen that the ratio does not exceed 2.5, which is sufficient for DNS quality resolution (Pope [24]). Maximum values of around 3 are reported in the recent DNS study of Hosseini *et al.* [25] around a NACA-4412 at $Re_c = 400,000$.

Figure 1b presents the mean streamwise velocity for the tripped flow. It can be seen that the aforementioned tripping method triggers early transition and indeed suppresses flow separation in the suction side.

III. Mathematical formulation of the resolvent operator

The Reynolds decomposition expresses the instantaneous velocity field as the sum of mean (time-average) and fluctuating fields $\boldsymbol{u} = \overline{\boldsymbol{u}} + \boldsymbol{u'}$. Substituting this decomposition into the Navier-Stokes equations and time-averaging we get the well-known Reynolds Averaged Navier-Stokes equations:

$$\overline{\boldsymbol{u}} \cdot \nabla \overline{\boldsymbol{u}} + \overline{\boldsymbol{u'} \cdot \nabla \boldsymbol{u'}} + \frac{1}{\rho}\nabla \overline{p} - \nu \nabla^2 \overline{\boldsymbol{u}} = 0, \tag{2}$$

$$\nabla \cdot \overline{\boldsymbol{u}} = 0. \tag{3}$$

Subtracting equations (2) and (3) from the instantaneous Navier-Stokes equations, we get the following equations for the fluctuating velocity and pressure:

$$\frac{\partial \boldsymbol{u'}}{\partial t} + \overline{\boldsymbol{u}} \cdot \nabla \boldsymbol{u'} + \boldsymbol{u'} \cdot \nabla \overline{\boldsymbol{u}} + \frac{1}{\rho}\nabla p' - \nu \nabla^2 \boldsymbol{u'} = -\boldsymbol{u'} \cdot \nabla \boldsymbol{u'} + \overline{\boldsymbol{u'} \cdot \nabla \boldsymbol{u'}}, \tag{4}$$

$$\nabla \cdot \boldsymbol{u'} = 0. \tag{5}$$

Equation (4) is non-linear and contains all the information of the original Navier-Stokes equations. The right hand side, denoted as $\boldsymbol{f'} = -\boldsymbol{u'} \cdot \nabla \boldsymbol{u'} + \overline{\boldsymbol{u'} \cdot \nabla \boldsymbol{u'}}$, can be considered as a forcing term that has a non-linear dependence on the output $\boldsymbol{u'}$. It contains the Reynolds

stresses, which in turn affect the time-average flow field, $\overline{\boldsymbol{u}}$. The input (forcing $\boldsymbol{f}'$) and the output $(\boldsymbol{u}', p')$ are therefore non-linearly coupled. This differs from the usual approach of characterising noise amplifier flows in which an imposed forcing is applied to the linearised Navier-Stokes equations (Schmid and Brandt [26], Sipp *et al.* [12], Sipp and Marquet [15], Lu and Papadakis [27]). In such a case, the forcing is external (i.e. independent of the output) and the linearised equations act as a transfer function that maps $\boldsymbol{f}'$ to $(\boldsymbol{u}', p')$.

If we assume however that the flow has reached a statistically steady state and that $\overline{\boldsymbol{u}}$ is known (and therefore not affected by the forcing $\boldsymbol{f}'$), then equations (4) and (5) indeed form a linear system. The central assumption is that $\overline{\boldsymbol{u}}$ is known. This approach has been proposed by McKeon and Sharma [7]. In such a case, equations (4) and (5) can be written in matrix form as:

$$\boldsymbol{B}\frac{\partial}{\partial t}\begin{pmatrix}\boldsymbol{u}'\\ p'\end{pmatrix} = \boldsymbol{L}\begin{pmatrix}\boldsymbol{u}'\\ p'\end{pmatrix} + \boldsymbol{P}\boldsymbol{f}', \tag{6}$$

where the following operators and matrices have been defined:

$$\boldsymbol{L} = \begin{pmatrix} -\overline{\boldsymbol{u}}\cdot\nabla() - ()\cdot\nabla\overline{\boldsymbol{u}} + \nu\nabla^2() & -\frac{1}{\rho}\nabla() \\ \nabla\cdot() & 0 \end{pmatrix} \tag{7}$$

$$\boldsymbol{P} = \begin{pmatrix}1\\0\end{pmatrix}, \qquad \boldsymbol{B} = \begin{pmatrix}1 & 0\\ 0 & 0\end{pmatrix}. \tag{8}$$

We consider a Fourier decomposition of the forcing $\boldsymbol{f}'$ and the output $(\boldsymbol{u}', p')$ in time and in the homogenous spanwise direction, z, i.e.

$$\boldsymbol{f}'(x,y,z,t) = \hat{\boldsymbol{f}}(x,y)e^{i(\omega t + k_z z)} + c.c. \tag{9}$$

$$\boldsymbol{u}'(x,y,z,t) = \hat{\boldsymbol{u}}(x,y)e^{i(\omega t + k_z z)} + c.c. \tag{10}$$

$$p'(x,y,z,t) = \hat{p}(x,y)e^{i(\omega t + k_z z)} + c.c. \tag{11}$$

where c.c. denotes complex conjugate.

In the present simulations, we consider only 2D disturbances, i.e. we take $k_z = 0$. This is justified by the fact that the dynamics of the naturally separating shear layer is dominated by the 2D amplification of the Kelvin-Helmholtz instabilities. The generation of the subharmonic is also a 2D phenomenon, originating from the non-linear interaction of the primary

instabilities, as explained in [28]. The vortex shedding in the wake also has a dominant 2D component. Equation (6) then becomes:

$$i\omega \boldsymbol{B} \begin{pmatrix} \hat{\boldsymbol{u}} \\ \hat{p} \end{pmatrix} = \boldsymbol{L} \begin{pmatrix} \hat{\boldsymbol{u}} \\ \hat{p} \end{pmatrix} + \boldsymbol{P}\hat{\boldsymbol{f}}, \tag{12}$$

If the forcing amplitude $\hat{\boldsymbol{f}}$ is assumed to be zero, we recover the generalized eigenvalue problem which is used to determine the stability characteristics of the time-averaged flow field (the eigenvalue would be $i\omega$). For non-zero forcing term, equation (12) can be written as:

$$\begin{pmatrix} \hat{\boldsymbol{u}} \\ \hat{p} \end{pmatrix} = \left(i\omega \boldsymbol{B} - \boldsymbol{L}\right)^{-1} \boldsymbol{P}\hat{\boldsymbol{f}}. \tag{13}$$

Pre-multiplying the left and right hand sides by $\boldsymbol{P}^T$ we can extract the velocity fluctuations $\hat{\boldsymbol{u}}$:

$$\hat{\boldsymbol{u}} = \boldsymbol{P}^T \left(i\omega \boldsymbol{B} - \boldsymbol{L}\right)^{-1} \boldsymbol{P}\hat{\boldsymbol{f}}, \tag{14}$$

The matrix $\boldsymbol{R}(\omega) = \boldsymbol{P}^T \left(i\omega \boldsymbol{B} - \boldsymbol{L}\right)^{-1} \boldsymbol{P}$ is the resolvent operator of the mean-flow and it is the focus of the analysis of the present work.

The discrete form of the operators and matrices appearing in (14) is obtained using the finite element package FreeFem++ [29]. The span- and time-averaged flow (obtained from DNS simulations) is interpolated to the nodes of a two-dimensional triangular finite element mesh that has very similar resolution as the finite volume DNS mesh. Standard Taylor-Hood P2-P1 elements are used for the velocity and pressure fields, with quadratic and linear shape functions, respectively. In the following we use $\boldsymbol{R}(\omega)$ to denote also the discrete form of the operator. For more details on how to derive the discrete form of $\boldsymbol{R}(\omega)$ using finite elements, refer to [15].

A. Calculation of the optimal forcings and responses

In the aforementioned context, the resolvent is the transfer function between the turbulent forcing $\hat{\boldsymbol{f}}$ and the velocity response $\hat{\boldsymbol{u}}$. It can be used to evaluate the spatial distribution of the forcing that will maximise the gain G of the system, defined as the ratio of two $\mathcal{L}_2$ norms:

$$G = \frac{\|\hat{\boldsymbol{u}}\|^2_{Q_u}}{\|\hat{\boldsymbol{f}}\|^2_{Q_f}} \tag{15}$$

where the subscripts Q_u and Q_f indicate that different weighting matrices can be used to define the forcing and response norms. For a general vector variable $\boldsymbol{y}$ in the domain Ω, the $\mathcal{L}_2$ norm is defined as the energy of the variable, $\|\boldsymbol{y}\|^2 = \int_\Omega \boldsymbol{y}^\dagger \boldsymbol{y} d\Omega$, where † denotes complex conjugate transpose. The discrete form is $\|\boldsymbol{y}\|^2 = \boldsymbol{y}^\dagger \boldsymbol{Q} \boldsymbol{y}$, where $\boldsymbol{Q}$ is a symmetric positive definite (or semi-definite) matrix, arising from the discretisation of the integral operator in the domain, and $\boldsymbol{y}$ is now the vector of discrete values of the variable (we use the same notation for the continuous variable and the vector of discrete values, but we hope that the distinction becomes clear from the context).

The discrete form of equation (15) can then be written as:

$$G = \frac{\hat{\boldsymbol{u}}^\dagger \boldsymbol{Q}_u \hat{\boldsymbol{u}}}{\hat{\boldsymbol{f}}^\dagger \boldsymbol{Q}_f \hat{\boldsymbol{f}}} \tag{16}$$

There is flexibility in the selection of the matrices $\boldsymbol{Q}_f$ and $\boldsymbol{Q}_u$. If the matrices define the energy in the whole domain, then $\boldsymbol{Q}_f = \boldsymbol{Q}_u = \boldsymbol{Q}$. However, this is not necessary. For example, $\boldsymbol{Q}_u$ can be selected to represent the energy only on a specific part of the domain, in which case $\boldsymbol{Q}_f \neq \boldsymbol{Q}_u$. Such a numerical experiment, with different $\boldsymbol{Q}_f$ and $\boldsymbol{Q}_u$ matrices, was performed in this work. For all cases examined, $\boldsymbol{Q}_f$ was defined in the whole domain, and therefore was invertible. Using the resolvent relation in (14), equation (16) becomes:

$$G = \frac{\hat{\boldsymbol{f}}^\dagger \boldsymbol{R}^\dagger \boldsymbol{Q}_u \boldsymbol{R} \hat{\boldsymbol{f}}}{\hat{\boldsymbol{f}}^\dagger \boldsymbol{Q}_f \hat{\boldsymbol{f}}} \tag{17}$$

The maximum value of G can be found directly by straightforward differentiation with respect to $\hat{\boldsymbol{f}}$:

$$\begin{aligned} \frac{\partial G}{\partial \hat{\boldsymbol{f}}} &= \frac{2\boldsymbol{R}^\dagger \boldsymbol{Q}_u \boldsymbol{R} \hat{\boldsymbol{f}} \hat{\boldsymbol{f}}^\dagger \boldsymbol{Q}_f \hat{\boldsymbol{f}} - 2\hat{\boldsymbol{f}}^\dagger \boldsymbol{R}^\dagger \boldsymbol{Q}_u \boldsymbol{R} \hat{\boldsymbol{f}} \boldsymbol{Q}_f \hat{\boldsymbol{f}}}{(\hat{\boldsymbol{f}}^\dagger \boldsymbol{Q}_f \hat{\boldsymbol{f}})^2} = \\ &= \frac{2}{\hat{\boldsymbol{f}}^\dagger \boldsymbol{Q}_f \hat{\boldsymbol{f}}} \left(\boldsymbol{R}^\dagger \boldsymbol{Q}_u \boldsymbol{R} \hat{\boldsymbol{f}} - G \boldsymbol{Q}_f \hat{\boldsymbol{f}} \right) = 0 \end{aligned} \tag{18}$$

Thus the forcing $\hat{\boldsymbol{f}}$ which maximises the gain G is the solution of the following generalized

eigenvalue problem:

$$\boldsymbol{R}^{\dagger}\boldsymbol{Q}_u\boldsymbol{R}\hat{\boldsymbol{f}} = G\boldsymbol{Q}_f\hat{\boldsymbol{f}} \tag{19}$$

This can be easily cast to a standard eigenvalue problem, because $\boldsymbol{Q}_f$ is invertible. The solution to this eigenproblem provides the squared singular values $\sigma_i^2 = G_i$ of the resolvent matrix $\boldsymbol{R}(\omega)$ and the corresponding weighted[1] right singular vectors, $\hat{\boldsymbol{f}}_i$. The left singular vectors $\hat{\boldsymbol{u}}_i$ are then given by:

$$\hat{\boldsymbol{u}}_i = \sigma_i^{-1}\boldsymbol{R}(\omega)\hat{\boldsymbol{f}}_i \tag{20}$$

The previous analysis indicates the physical significance of the right and left singular vectors. At a given frequency ω, the former correspond to the forcing which will maximise the response of the system under the defined norm, while the latter correspond to the response itself. The gain of the system, i.e. the ratio of the norms, will then be G. The right and left singular vectors that result in the highest singular value -i.e. those which produce the largest gain - will be referred from now on as the optimal forcing and optimal response respectively.

It is straightforward to show that the forcings $\hat{\boldsymbol{f}}_i$ and responses $\hat{\boldsymbol{u}}_i$ form bases of their corresponding spaces and thus any arbitrary forcing and response can be written as a linear combination of these base members. Thus any forcing $\boldsymbol{f}$ can be expressed as a weighted sum of the base forcings $\hat{\boldsymbol{f}}_i$ as;

$$\hat{\boldsymbol{f}} = \sum_{i=1}^{N}\langle\hat{\boldsymbol{f}}, \hat{\boldsymbol{f}}_i\rangle\hat{\boldsymbol{f}}_i \tag{21}$$

where N is the number of singular modes and $\langle\hat{\boldsymbol{f}}, \hat{\boldsymbol{f}}_i\rangle = \hat{\boldsymbol{f}}^{\dagger}\boldsymbol{Q}_f\hat{\boldsymbol{f}}_i$ denotes the projection of the arbitrary forcing $\boldsymbol{f}$ to the i^{th} forcing mode. Then, using equations (14) and (20), the corresponding response $\hat{\boldsymbol{u}}$ to the arbitrary forcing $\hat{\boldsymbol{f}}$ can be expressed as:

$$\hat{\boldsymbol{u}} = \sum_{i=1}^{N}\sigma_i\langle\hat{\boldsymbol{f}}, \hat{\boldsymbol{f}}_i\rangle\hat{\boldsymbol{u}}_i \tag{22}$$

In many shear flows, and depending on the examined frequency, the first singular value, σ_1, can be orders of magnitude larger than the rest (McKeon and Sharma [7], Beneddine *et al.* [11]). This means that the first term in the right hand side of equation (22) is expected

[1] In the standard SVD, the left and right singular vectors satisfy $u_i^{\dagger}u_j = \delta_{ij}$ and $v_i^{\dagger}v_j = \delta_{ij}$, where δ_{ij} is the Kronecker symbol. However, in the weighted SVD they satisfy $u_i^{\dagger}\boldsymbol{Q}_u u_j = \delta_{ij}$ and $v_i^{\dagger}\boldsymbol{Q}_v v_j = \delta_{ij}$, where $\boldsymbol{Q}_u$ and $\boldsymbol{Q}_v$ are weighting matrices [30].

to dominate over the rest. The implicit assumption is that the arbitrary forcing $\hat{\boldsymbol{f}}$ will be such that $|\sigma_1\langle\hat{\boldsymbol{f}},\hat{\boldsymbol{f}}_1\rangle| \gg |\sigma_i\langle\hat{\boldsymbol{f}},\hat{\boldsymbol{f}}_i\rangle| \quad (i = 2...)$, i.e. the relative magnitude of the first term compared to the second, third etc is dictated by the order of singular values σ_i and the projection of $\hat{\boldsymbol{f}}$ to second, third etc base members $\hat{\boldsymbol{f}}_i$ will not be so strong as to reverse this order. In section V, we will use the dominance of the first term to model the velocity spectra based on the estimation of the coefficient $\langle\boldsymbol{f},\hat{\boldsymbol{f}}_1\rangle$ for each frequency.

The eigenproblem (19) was solved using an in-house code, which employed the ARPACK library for the computation of a few large eigenvalues (Lehoucq *et al.* [31]), coupled with the MUMPS package for the efficient LU decomposition and solution of large sparse matrices (Amestoy *et al.* [32]).

IV. Resolvent analysis

A. Naturally developing flow around an airfoil with straight trailing edge

The spectrum of the resolvent operator for the 5 largest growth ratios is shown in Figure 4. The largest G, corresponding to the dominant singular value σ_1, is 7 orders of magnitude larger than the second for a wide range of frequencies. This strong amplification is a characteristic feature of the convectively unstable nature of the separated shear layer which forms on the suction side of the airfoil. A similar behaviour has been observed in other flows which exhibit a strong convective instability (Beneddine *et al.* [11],Sipp *et al.* [12],Garnaud *et al.* [33],Alizard *et al.* [14]).

As it can be seen in Figure 4, the optimal growth reaches its highest value at the angular frequency ω_P, which is very close to the natural frequency of the separated shear layer, denoted as $\omega_2 = 2\pi f_p$, where $f_2 = 7.4$ as found in Thomareis and Papadakis [20]. Indeed ω_2 is approximately 7.8% larger than ω_P. This is a good estimation of the shear layer natural frequency, bearing in mind that only the time-averaged velocity has been used in the simulations, and the flow undergoes laminar separation, transition, turbulent reattachment and contains a turbulent wake.

The overall shape of the resolvent spectrum resembles that of a band-pass filter, centred approximately at the shear layer frequency ω_2. Indeed past studies, such as those by Jones *et al.* [34], Desquesnes *et al.* [35] and Rodriguez and Theofilis [36], identified a frequency

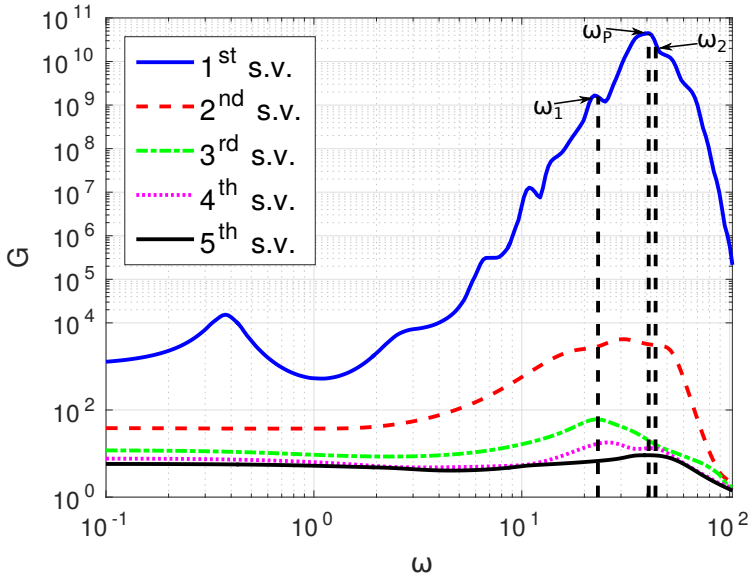

FIG. 4: Spectrum of the resolvent operator for the naturally developing flow around a NACA-0012 with straight trailing edge. The first 5 gain values of the operator are plotted against the angular frequency ω.

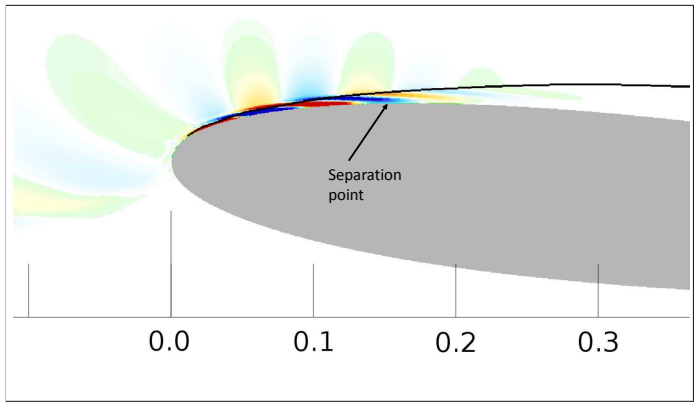

FIG. 5: Streamwise component of the optimal forcing $\hat{f}_x$ at frequency ω_P at the leading edge with the displacement thickness of the boundary layer superimposed. The contours range is $[-72, 72]$.

selection mechanism in laminar separation bubbles, according to which the separation bubble will selectively amplify frequencies around the dominant frequency of the shear layer, thus acting as a band-pass filter.

Both components of the optimal forcing are found to be localized in the leading edge of the airfoil, with their magnitude decaying rapidly downstream. The real part of the streamwise component at frequency ω_P is plotted together with the displacement thickness of the boundary layer in figure 5. The plot is zoomed-in close to the leading edge. Forcing is dom-

inant in the area of maximum acceleration. The separation point is located at $x/c = 0.145$ and the forcing attains its maximum value slightly upstream of this location. The structure of the forcing, and more specifically the inclination opposite to that of the mean shear, suggests that the Orr mechanism is responsible for amplifying the disturbances upstream of separation. According to this mechanism, perturbations that are initially tilted opposite to the shear, extract energy from the mean flow by transporting momentum through the action of the perturbation shear stress. As the structures are advected to a more upright position, the perturbation gains energy. Butler and Farrell [37] studied the optimal perturbations in three model flows (Couette flow, Poiseuille flow and a Blasius boundary layer) and found that the 2D initial condition that would give the maximum amplification had a very similar structure. The optimal forcing in attached flat plate boundary layer flows has also the same shape ([13] and [15]).

Apart from the wall, it is very interesting to notice the presence of forcing in the free steam as well. This indicates that natural disturbances (in a physical setting) or discretisation errors (in a computational setting) upstream of the airfoil provide the seeds that trigger the Kelvin-Helmholtz instability in the separating shear layer. In the Blasius boundary layer resolvent simulations of [15] that include the flow upstream and around the leading edge of the flat plate, only the forcing in the near wall region appears (figure 2 in the paper). This is probably due to the fact that in a separating boundary layer, the growth of disturbances is much higher; indeed the local stability analysis of Dovgal *et al.* [38] reports more than an order of magnitude higher growth rate when back flow in present. In such conditions, even small free stream disturbances are significantly amplified, and this can explain the spatial presence of forcing in the free-stream.

The real part of the cross-stream component of the optimal response close to the airfoil is shown in Figure 6. The displacement thickness of the suction side boundary layer (solid black line) and the zero streamwise mean velocity contour (solid brown line) are also shown. The imaginary part (not shown here) is very similar, but displaced in the streamwise direction (the two parts when substituted in equation (10) result in the propagation of the perturbation in the streamwise direction). The results are indicative of the convectively unstable nature of the flow field. There is a clear cause-and-effect relation between the forcing, localised upstream, and the corresponding response further downstream. The forcing leads to a response which is gradually amplified in the separated shear layer and reaches a local

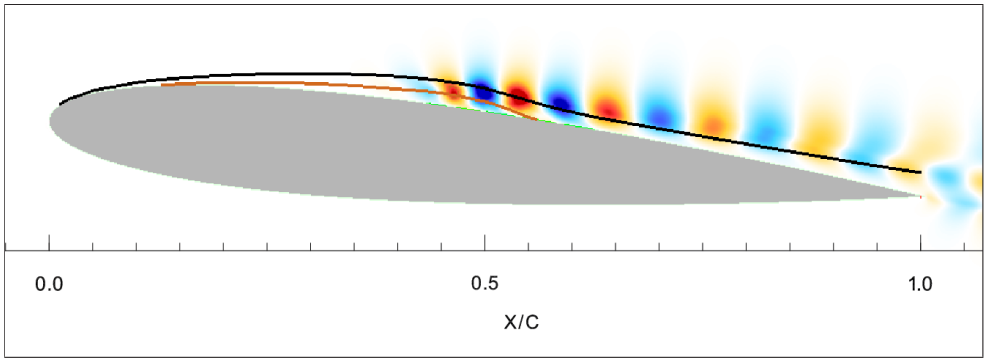

FIG. 6: Cross-stream component of the optimal response at frequency ω_P at the suction side of the airfoil. The solid black line shows the displacement thickness of the boundary layer while the solid brown line is the zero-streamwise mean velocity contour. The contours range is $[-4.17, 4.17]$.

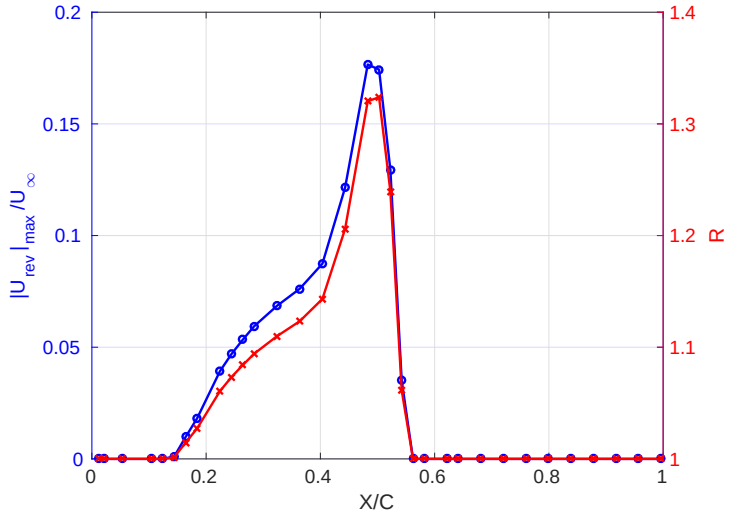

FIG. 7: Absolute value of the maximum reverse flow (blue line-left axis) and velocities ratio R (red line-right axis), over the airfoil's suction side.

maximum value at reattachment ($x/c = 0.56$). Further downstream, the attached boundary layer causes a significant attenuation of the response.

This plot demonstrates that the response grows rapidly at the downstream end of the recirculation zone. Indeed, the growth of the disturbance is very closely correlated with the maximum reverse flow observed in the separation bubble. In Figure 7 the maximum reverse flow and the velocity ratio R are plotted in the suction side. In a mixing layer, the velocity ratio is defined as $R = \frac{U_1 - U_2}{U_1 + U_2}$, where U_1 and U_2 are the velocities of the two streams. In the current setting, these are the free stream velocity and the maximum reverse velocity respectively at each x/c location. The rapid growth of the response in Figure 6, which

takes place at approximately $x/c = 0.4$, closely matches the location of the rapid increase of the reverse flow seen in Figure 7. The effect of the strength of the reverse flow on the amplification rate of the disturbances has been found in the past ([38]). Strykowski and Niccum [39] found a significant increase in the amplitude of velocity oscillations, in a mixing layer when the velocity ratio R is larger than 1 (counter-current mixing layer) compared to the case where $R < 1$ (co-flowing mixing layer), with an even larger increase as this ratio exceeds the critical value of approximately $R = 1.3$. In Figure 7 the velocities ratio appears to be close to this critical value and even exceed it at a small area. Despite the fact that the flow studied by Strykowski and Niccum [39] (a parallel mixing layer) is different from the one examined in the present work, the results appear to agree and to justify, at least in a qualitative sense, the location where the disturbances are rapidly amplified.

The aforementioned characteristics are entirely consistent with the DNS results. Indeed the DMD mode obtained directly from the processing of instantaneous snapshots of the flow (figure 9(b) in [20]) shows a striking similarity to figure 6. Note that the normalisation used in the DMD and the resolvent modes are different, so it is appropriate to compare the shape only. The location of inception of the mode, the number and distance between the counter rotating vortices, and the attenuation close to the trailing edge, are features that match almost perfectly. For example, upstream of the reattachment point where the response has the largest amplitude, the wavelength of the counter rotating vortices is $0.08C$, exactly as in the DMD mode. There are slight differences close to the trailing edge; the DMD mode appears more rugged, while in figure 6 it is very smooth. This is because of the finite number of snapshots used to construct the DMD mode, and the fact that the snapshots were obtained in one spanwise plane, i.e. were not spanwise averaged. In the resolvent analysis, the 2D modes are computed directly from the Navier-Stokes equations, leading to smoother results. The theoretical link between the resolvent and DMD modes has been explored recently for general flow configurations as well as configurations with spatial invariance in [9].

Attention is now turned to the optimal mode at the subharmonic frequency $f_1 = 3.8$ (the corresponding angular frequency ω_1 is denoted in figure 4). The DNS simulations indicate that f_1 is dominant in the aft part of the airfoil and the wake ([20]). The origin of this frequency is explained, among other papers, in [28]. It arises when the primary frequency has reached saturation. If one performs linear stability analysis around the periodic base

flow (consisting of the time-average plus the periodic primary velocity field), then the sub-harmonic is the only mode that can reproduce itself through non-linear interaction with the base flow. Again this is a 2D mode. One can potentially perform resolvent analysis in a periodic base flow (instead of a time-average) and explore if this mode also becomes dominant, as the DNS simulations demonstrate. The periodic component can be obtained by phase- and spanwise-averaging of the instantaneous DNS snapshots. We have not pursued this direction in the present paper, instead we have used the mean-flow only, as is customary in resolvent analysis. However, this explains why the growth predicted at this frequency is about one order of magnitude smaller than that of the fundamental shear layer frequency (refer to figure 4). The optimal response is shown in Figure 8. The response is visible in the aft part of the airfoil, but has a much stronger presence in the wake (this again agrees with the DNS findings). The wavenumber of the structures is half compared to that of figure 6, a result which is expected due to the lower temporal frequency.

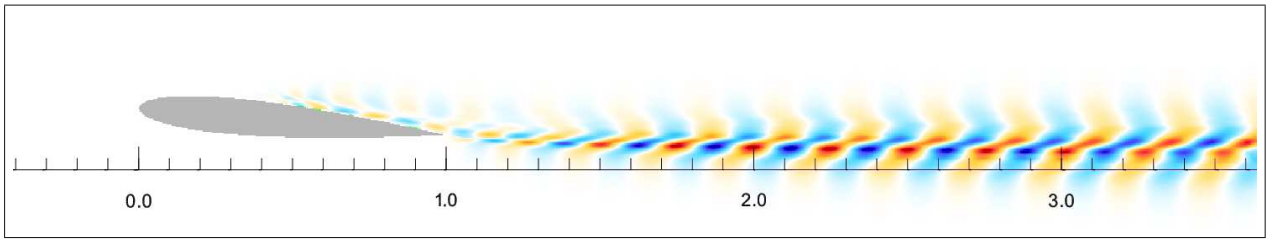

FIG. 8: Streamwise component of the optimal response $\hat{u}_x$ at the wake shedding frequency ω_1. The contours range is $[-4.1, 4.1]$.

B. Naturally developing flow around an airfoil with blunt trailing edge

In Figure 9 the resolvent spectra for both blunt and straight trailing edge airfoils are plotted together. Again for this flow, the second highest singular value (not shown in the figure) is 4 orders of magnitude smaller than the first. The two spectra show a similar overall behaviour, with one important and interesting difference. For the straight trailing airfoil, the shear layer has the highest receptivity in the range of frequencies $\omega = 20 - 60$. In the this range however, the gain is almost an order of magnitude smaller for the blunt trailing edge airfoil. The presence of bluntness therefore renders the separated shear layer much less receptive to forcing compared to the straight trailing edge case. There are also some differences in the spectra for very low frequencies, but the gain at these frequencies is many

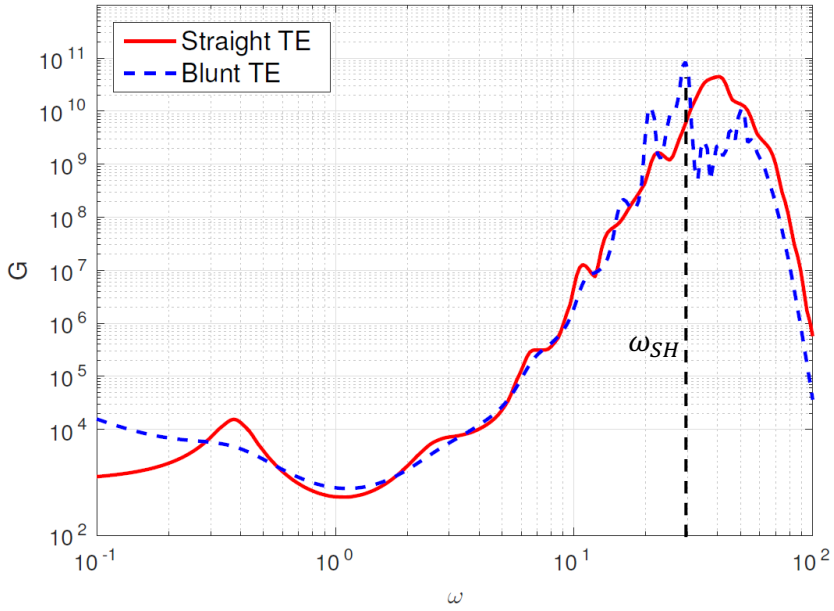

FIG. 9: Resolvent spectra of the straight and blunt trailing edge cases.

orders of magnitude smaller.

A pronounced peak at $\omega_{SH} = 29.3$ is observed, which almost perfectly matches the vortex shedding frequency $\omega = 28.26$ found in [20]. After this peak, a few local extrema are observed, and then the gain decays rapidly for frequencies larger than approximately $\omega = 60$.

The optimal forcing for this case is very similar to that of the straight trailing edge airfoil. The structures are tilted opposite to the mean shear, indicating that the Orr-mechanism is responsible for the growth of perturbations. The cross-stream component of the corresponding optimal response, shown in Figure 10, is concentrated in the wake of the airfoil. This is a direct result of the Kárman shedding originating from the truncated trailing edge. The mode is present at the suction side of the airfoil, albeit highly attenuated. The shape of this mode is again qualitatively similar to the dominant DMD mode found for the same flow configuration (figure 12(b) in [20]), with highly energetic structures originating from the truncated part of the trailing edge and propagating downstream.

In the DNS simulations it was found that in the presence of vortex shedding from the blunt edge the natural frequency of the separating shear layer was suppressed, and instead the new shear layer frequency was locked to the shedding frequency. This lock-in mechanism

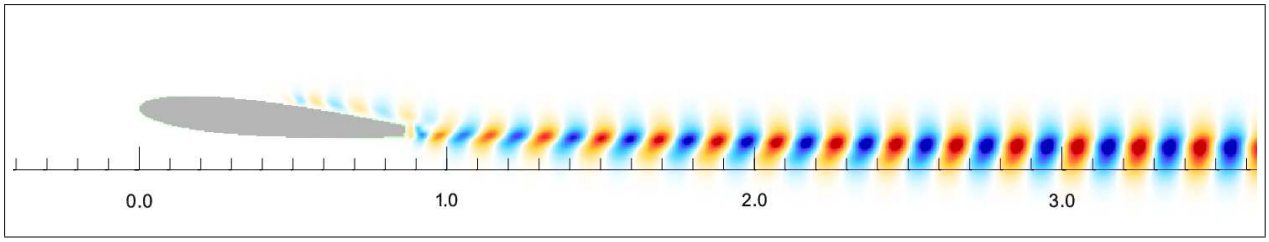

FIG. 10: Cross-stream component of the optimal response $\hat{u}_y$ at the vortex shedding frequency ω_{SH}. The contours range is $[-3.59, 3.59]$.

can explain the observed suppression of the sensitivity of the separated shear layer to forcing. It is very interesting that the resolvent analysis can capture this feature.

The change in the dominant frequency in the separating shear layer is reflected in the structure of the response. In figure 11 we zoom into the response in the suction side of the airfoil for angular frequency ω_{SH} (this is equivalent to figure 6 for the straight trailing edge). Comparing the two plots, it can be seen that the Kelvin-Helmholtz structures are more widely apart, as expected. We have also investigated the shape of the maximum reverse flow (not shown), and it was found to be very similar to that of the straight trailing edge case, but the values are slightly smaller (15% of U_∞ as opposed to approximately 17.6% of U_∞).

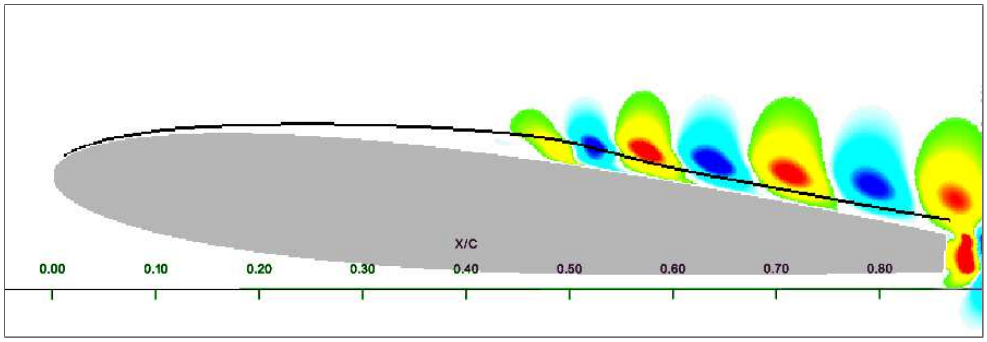

FIG. 11: Cross-stream component of the optimal response at the suction side of the airfoil at frequency ω_{SH}. The solid black line shows the displacement thickness of the boundary layer. The contours range is $[-0.8, 0.8]$.

C. Tripped airfoil with straight trailing edge

1. *Analysis of the tripped flow*

In the flow around the blunt trailing edge airfoil, the sensitivity of the separating shear layer to external forcing was reduced because it was locked to vortex shedding. This provides the motivation for additional simulations in which the flow in the suction side is attached. To suppress separation, the flow is artificially tripped. Details about the tripping mechanism and the numerical implementation were provided in section II. Figure 1 in that section demonstrated that a result of the artificial tripping, the separating bubble is indeed suppressed and the boundary layer remains attached (in a time-average sense).

In order to provide more insight into the instantaneous flow field close to the wall, we computed the probability density function (PDF) of the skin friction C_f and pressure coefficients C_P over the suction surface. The samples were collected in the spanwise direction and over time. The PDF's were computed at 200 points in the suction side and 29 bins were used at each point. Due to the large variation of both C_P and C_f from the leading to the trailing edge, using the same bins at each location does not give satisfactory results. For this reason, at each point x/c, the size of the bins was scaled so that they cover a spread between $-3\sigma(x)$ and $+3\sigma(x)$ around the mean value $\mu(x)$, where $\sigma(x)$ is the standard deviation at x [40]. The number of samples in each bin is then normalised with the bin area $\delta x \delta C_{f,P}$ and the total number of samples across all bins at the segment $[x, x+\delta x]$. While the segments in the streamwise direction have uniform length $\delta x = c/199$, the size of the bins $\delta C_{f,P}$ depends on $\sigma(x)$ and is given by $\delta C_{f,P} = \frac{6}{29}\sigma(x)$.

Figures 12a and 12b show the PDF of skin friction coefficient for the flows with and without tripping. The extent along the vertical axis is a measure of the variance, thus the locations where the PDF appears to be a single line are regions of very low variance and thus almost steady flow. On the other hand, regions where the values of the PDF are more spread out imply higher temporal and spanwise variation of C_f. In the naturally developing boundary layer, as figure 12a suggests, the values are to a large extent almost steady until approximately $x/c = 0.4$; downstream of this point the shear layer shedding intensity starts to grow rapidly. In the tripped case, shown in Figure 12b, the perturbations introduced close to the leading edge lead to an initially larger spread of C_f values. However closer to

what would be the separation point, the difference between the two figures is striking, the spread of C_f is much smaller and the range of values much more clustered around the mean.

The pressure coefficient plots, shown in figures 12c and 12d, show the same behaviour. While the time-average pressure remains constant inside the recirculation zone (pressure plateau between approximately $x/c = 0.2$ and 0.55), the spread around the mean is quite large. In the tripped case, C_P follows a gradual recovery towards the free stream pressure, leading to an adverse mean pressure gradient in the whole suction side. The spread around this time-average distribution is significantly reduced compared to the naturally developing flow. An interesting feature in figure 12b is the presence of a region, approximately between $x/c = 0.15 - 0.3$, where the average C_f value is almost zero (it can be seen that the PDF is symmetrically placed around zero). The negative values of C_f imply the presence of instantaneous flow reversal appearing locally, which indicates the presence of incipient separation of the boundary layer.

Figure 13a shows the tangential velocity profiles in x/c=0.01-0.32. Shortly downstream of the tripping strip (located at $x/c = 0.04 - 0.06$), the profiles become very distorted and inflectional close to the wall. At this region, the transition induced by the tripping competes with the adverse pressure gradient. The latter reduces the slope of the profile close to the wall, but the flow never separates (in a time average sense) because of the transition induced by the tripping. In the region $x/c = 0.16 - 0.32$, the profiles approach the wall almost vertically (indicating mean $C_f \approx 0$). Further downstream the flow re-accelerates and the distortion is to a large extent eliminated (Figure 13b).

Point spectra at two locations, $x/c = 0.47$ and $x/c = 0.68$, are shown in Figure 14 and demonstrate the presence of a shedding mode, which develops from an initial high frequency of approximately $f_{2,Trip} = 9.0$ at the mid-point of the suction side, to its half-subharmonic $f_{P,Trip}$ from about $x/c = 0.6$ and further downstream into the wake.

The presence of the inflectional profiles seen in Figure 13a provides the inviscid mechanism by which the flow can become unstable to perturbations and can explain the presence of the high frequency noted in the spectra. A snapshot of the instantaneous streamwise velocity field can be seen in Figure 15. A set of vortices can be easily identified (delineated with red half-circles).

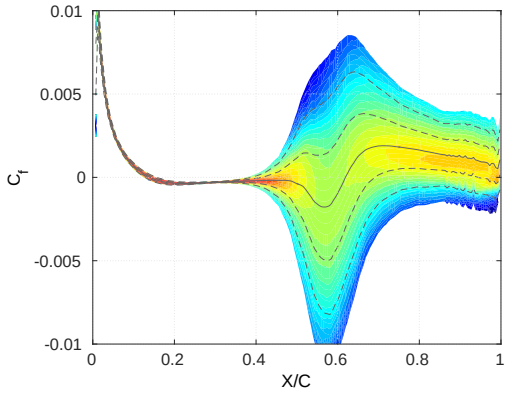

(a) C_f (naturally developing flow)

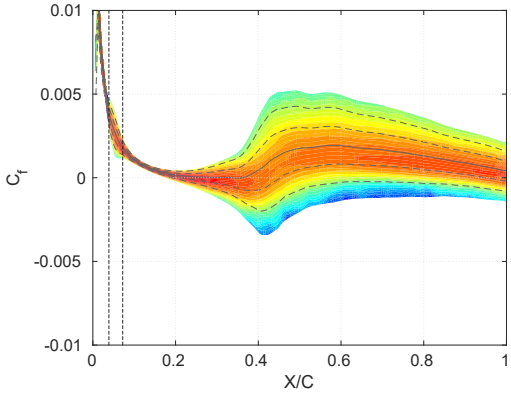

(b) C_f (tripped flow)

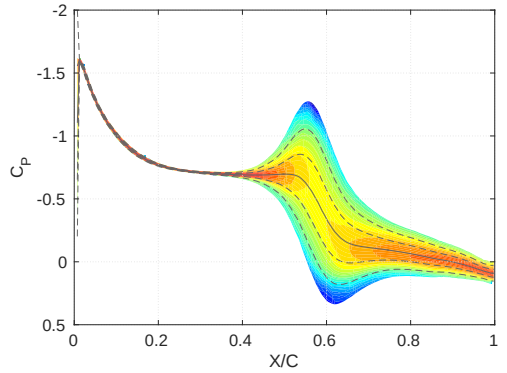

(c) C_P (naturally developing flow)

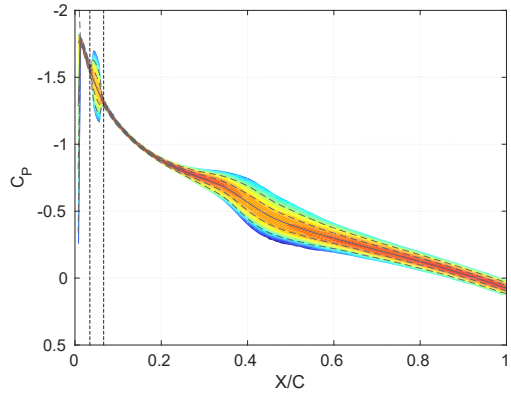

(d) C_P (tripped flow)

FIG. 12: Probability density function of C_f and C_P for the naturally developing (left column) and tripped (right column) flows. The solid line in each plot denotes the mean value, while the dashed lines bracket the $\pm 1\sigma$ and $\pm 2\sigma$ ranges around the mean. The vertical dashed lines in figures 12b and 12d indicate the thin strip where tripping was applied.

2. *Resolvent analysis of the tripped flow*

The absence of reverse flow greatly impedes the amplification characteristics of the Kelvin-Helmholtz mechanism which is in place both in the untripped and in the tripped cases. It it thus expected that this will affect the response characteristics of the flow-field. The spectrum of the resolvent operator is shown in Figure 16. Three important differences with respect to the naturally developing flows can be observed.

Firstly, the peak is suppressed by almost two orders of magnitude with respect to the blunt trailing edge airfoil, and more than one order of magnitude with respect to the straight

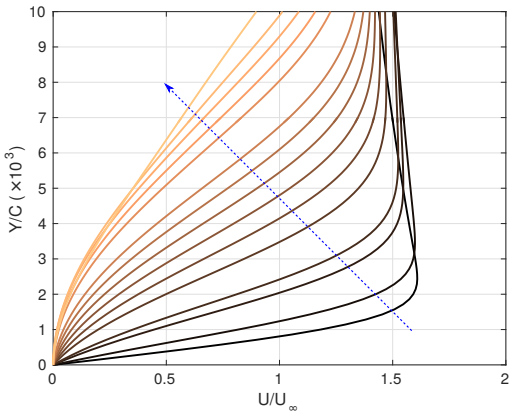

(a) Velocity profiles at x/c=0.01, 0.02, 0.05, 0.1, 0.12, 0.14, 0.16, 0.18, 0.22, 0.24, 0.26, 0.28, 0.32.

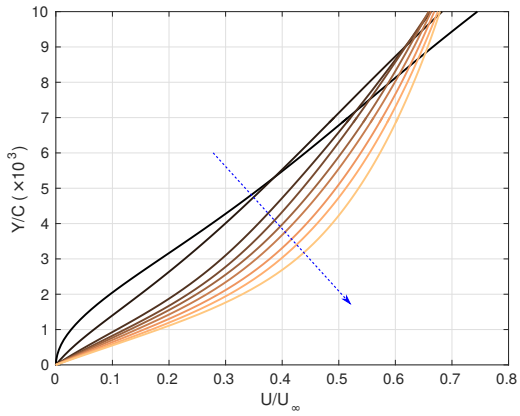

(b) Velocity profiles at x/c=0.40, 0.44, 0.48, 0.50, 0.52, 0.54, 0.56, 0.58, 0.62

FIG. 13: Tangential velocity profiles at the airfoil's surface (shown up to $Y/C = 0.01$). The dashed blue arrows indicate increasing x/c.

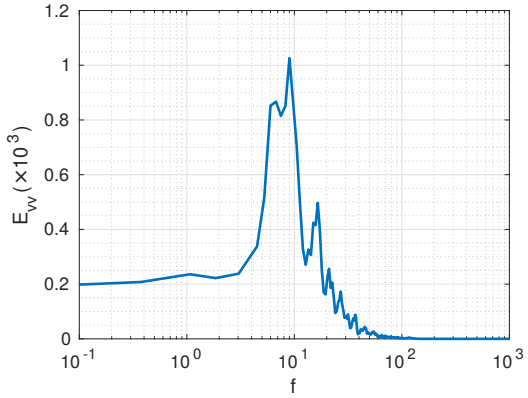

(a) $X/C = 0.47$,$Y/C = 0.035$.

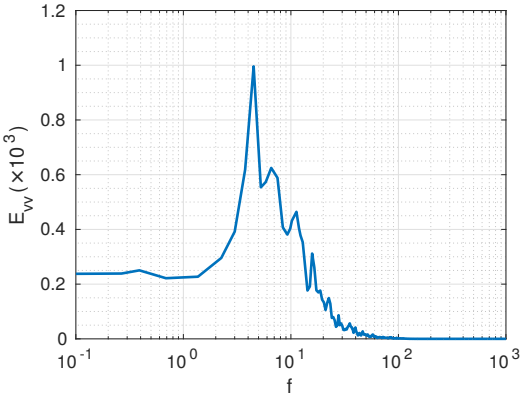

(b) $X/C = 0.68$,$Y/C = 0.012$.

FIG. 14: Cross-stream velocity spectra at two locations on the suction' side boundary layer.

trailing edge. This indicates that the growth of perturbations is significantly reduced with respect to both naturally developing flows that exhibit recirculation. The reduction is larger with respect to the blunt airfoil, because in this case the whole flow is locked to the shedding frequency. Secondly, the location of the peak has shifted. While in the previous two flows, the peak was located at the natural frequency of the separated shear layer, in the tripped flow it is located close to the sub-harmonic frequency (at $\omega_{P,Trip} = 30$ or $f_{P,Trip} = 4.77$, 6% difference with the sub-harmonic found earlier from processing the DNS time series). This frequency however develops downstream of the airfoil and into the wake. Thirdly, there is

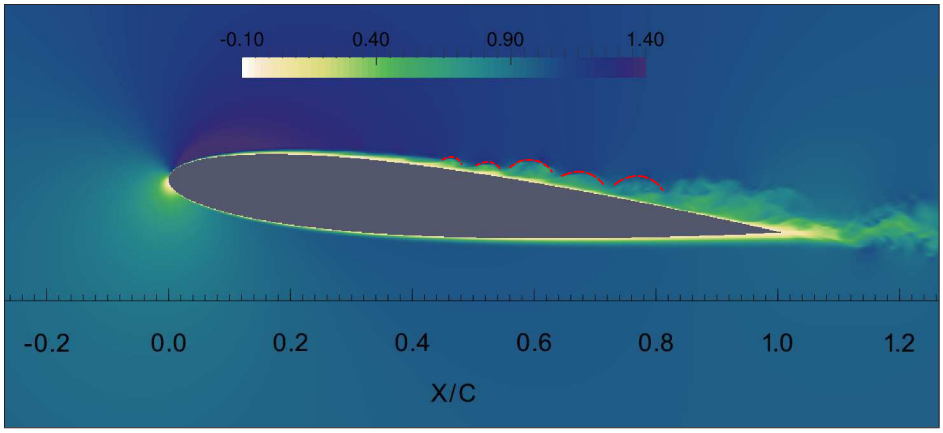

FIG. 15: Instantaneous streamwise velocity field. The red curves delineate large scale structures.

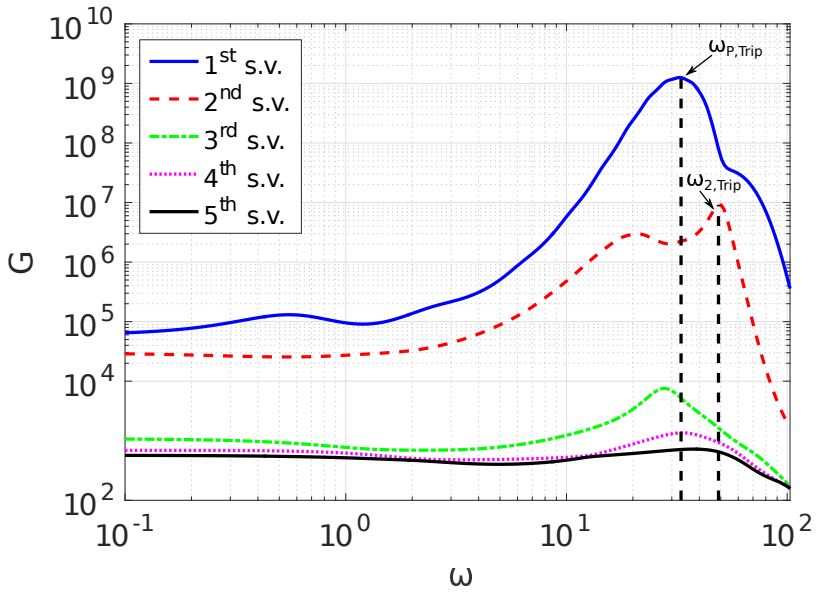

FIG. 16: Resolvent spectrum for the tripped straight trailing edge airfoil.

no clear separation between the first and second singular values; the latter (denoted by a red dashed line) is now much closer to the former, implying a higher contribution in the full response. It also peaks at the frequency of the shedding originating the suction side, at approximately $\omega_{2,Trip} = 56$ or $f_{2,Trip} = 9.0$, found earlier.

The optimal forcing in the cross-stream direction at frequency $\omega_{P,Trip}$ is shown in figure 17. The forcing appears not only in the area of high acceleration in the suction side (as in the previous two cases) but also in the aft part of the pressure side (with reduced amplitude). The flow in this side is still laminar; we have checked the Reynolds stresses and they

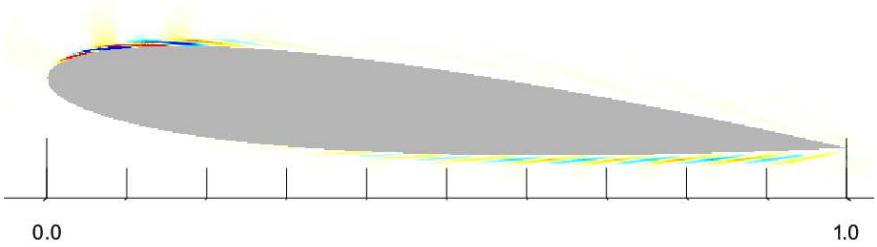

FIG. 17: Optimal forcing in the cross stream direction at frequency $\omega_{P,Trip}$. The contours range is $[-69.2, 69.2]$

are negligible. The spatial structure of the optimal forcing is opposed to the mean shear, indicating the Orr mechanism is acting on both sides.

The spatial structure (cross-stream components) of the two modes corresponding to the aforementioned peaks is shown in Figure 18. The lowest frequency at $\omega_{P,Trip} = 30$ is indeed amplified in the wake whereas the highest frequency $\omega_{2,Trip}$ is present in the boundary layer in the suction side and then gradually decays in the wake.

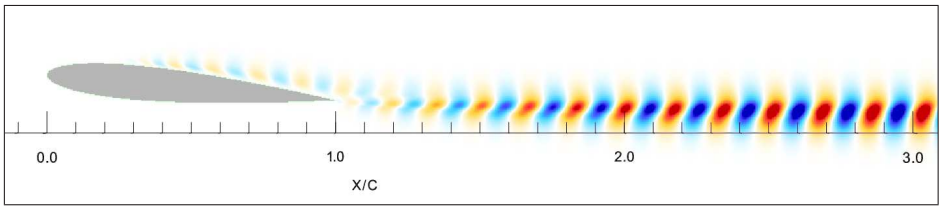

(a) Response at $\omega_{P,Trip}$ (highest singular value).

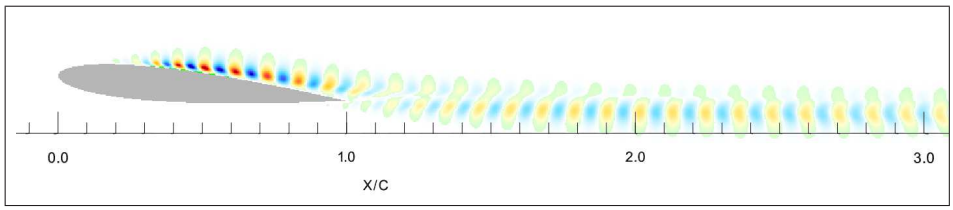

(b) Response at $\omega_{2,Trip}$ (second singular value).

FIG. 18: Cross-stream components of responses at frequencies $\omega_{P,Trip}$ and $\omega_{2,Trip}$. The contours in figure 18a range between $[-3.6, 3.6]$ while in figure 18b $[-9.8, 9.8]$.

The close proximity of the two singular values motivates the examination of the effect of the optimization domain. It was shown in section III A that the outcome of the resolvent analysis depends on the area at which the response is maximised; this is determined by the matrix $\boldsymbol{Q}_u$. We repeated the resolvent analysis, this time maximising the response in the domain shown in Figure 19 (the elements of matrix $\mathbf{Q_u}$ were set to 0 outside this area).

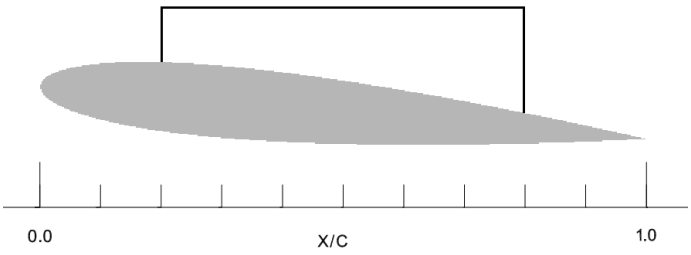

FIG. 19: Optimization domain defined on the suction side of the airfoil.

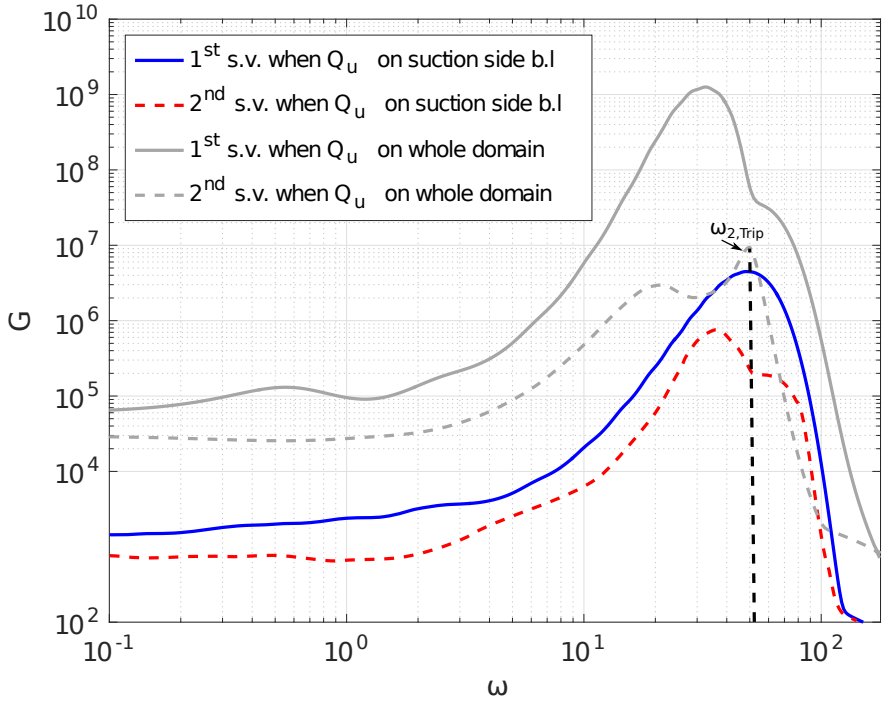

FIG. 20: Resolvent spectra with different optimization domains. The grey lines correspond to optimisation over the whole domain, while the coloured lines correspond to a domain on the suction side of the airfoil.

The resulting spectrum of the resolvent operator is shown in Figure 20, superimposed on the spectrum computed in the whole domain. The singular values are now much smaller, as expected. The dashed line indicates the frequency $\omega_{2,Trip}$. A noticeable difference in Figure 20, when compared with Figure 16, is that the location of the peaks is reversed. The dominant singular value now peaks at $\omega_{2,Trip}$, whereas the second one peaks closer to $\omega_{P,Trip}$. Figure 21 shows the spatial distribution of the optimal mode at $\omega_{2,Trip}$, and of course this is indeed localized at the boundary layer on the suction side, as expected.

The previous analysis demonstrates that in the tripped case, the outcome of the resolvent analysis depends on the optimization domain. When the whole domain is used, the disturbance with the highest energy gain beats at frequency $\omega_{P,Trip}$ and is located in the wake. When the domain is restricted on the suction side the optimal response pulses at frequency $\omega_{2,Trip}$. It is worth mentioning that in the two untripped cases, the first singular value peaked at the shear layer frequency, even when the whole domain was used. This was due to the very strong amplifying characteristics of the separating shear layer. When the flow is tripped, the flow remains attached, and the growth of perturbations becomes significantly suppressed. In this case, the effect of wake predominates and shifts the location of the peak of the first singular value.

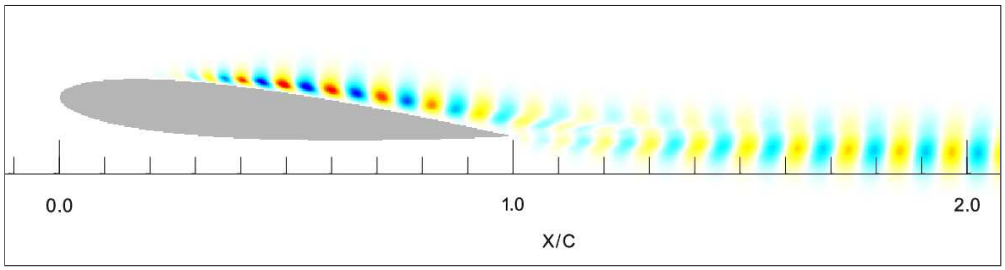

FIG. 21: Cross-stream component of the optimal response at the frequency $\omega_{2,Trip}$ when the domain shown in Figure 19 is used in the optimization process. The contours range is $[-7.7, 7.7]$.

V. Estimation of velocity spectra based on point measurements

As shown in section III A, the response $\hat{\boldsymbol{u}}$ of the flow field to any forcing $\hat{\boldsymbol{f}}$, can be written as (equation (22) repeated below):

$$\hat{\boldsymbol{u}} = \sum_{i=1}^{N} \sigma_i \langle \hat{\boldsymbol{f}}, \hat{\boldsymbol{f}}_i \rangle \hat{\boldsymbol{u}}_i \tag{23}$$

If the first singular value is orders of magnitude larger than the others, the first term in the sum of equation (23) will dominate (provided of course that the forcing has appreciable projection to the optimal forcing $\hat{\boldsymbol{f}}_1$). In this case, the response can be approximated by:

$$\hat{\boldsymbol{u}} = \sigma_1 \langle \hat{\boldsymbol{f}}, \hat{\boldsymbol{f}}_1 \rangle \hat{\boldsymbol{u}}_1 \tag{24}$$

The only unknown in equation (24) is the term $\langle \hat{\boldsymbol{f}}, \hat{\boldsymbol{f}}_1 \rangle$ which is the projection of the turbulent forcing $\boldsymbol{f}$ onto the optimal forcing vector $\hat{\boldsymbol{f}}_1$. The forcing $\hat{\boldsymbol{f}}$ contains the non linear part of the Navier-Stokes equation (4), which is unknown, thus the projection $\langle \hat{\boldsymbol{f}}, \hat{\boldsymbol{f}}_1 \rangle$ cannot be calculated. If we define the scalar $\Psi = \sigma_1 \langle \hat{\boldsymbol{f}}, \hat{\boldsymbol{f}}_1 \rangle$ then Ψ is only a function of the frequency ω, $\Psi = \Psi(\omega)$. Making the dependence of each variable in equation (24) explicit, we get:

$$\hat{\boldsymbol{u}}(\boldsymbol{x}, \omega) = \Psi(\omega) \hat{\boldsymbol{u}}_1(\boldsymbol{x}, \omega) \tag{25}$$

$\Psi(\omega)$ is unknown, but the spatial distribution of $\hat{\boldsymbol{u}}_1$ is known for every frequency. Thus if we probe the i-th velocity component at a point $\boldsymbol{x}_0$, $\hat{\boldsymbol{u}}^{(i)}(\boldsymbol{x}_0, t)$, and take the Fourier transform of the signal, we can calculate $\Psi(\omega)$ by solving (25) to get:

$$\Psi(\omega) = \frac{\hat{\boldsymbol{u}}^{(i)}(\boldsymbol{x}_0, \omega)}{\hat{\boldsymbol{u}}_1^{(i)}(\boldsymbol{x}_0, \omega)} \tag{26}$$

Having estimated $\Psi(\omega)$ for each ω, an estimation of the spectrum of the velocity at an arbitrary point $\boldsymbol{x}$ can be obtained from equation (25).

This approach has been used recently with very promising results. Beneddine *et al.* [11] used this method to estimate the velocity spectra at several points on a backward facing step flow, and to reconstruct the dynamics of a round jet from PIV data [41]. Gómez *et al.* [19] used a variation of this method to estimate the forces acting on an inclined square cylinder. The coefficients in the latter application were computed in the time domain.

In the present study, we apply this method to estimate the spectra in the two regions of interest of the flow field, the suction side of the airfoil and the wake. In Figure 22 the DNS spectra of the cross-stream velocity are plotted along with the spectra estimated using equation (25), for the straight trailing edge airfoil. The function $\Psi(\omega)$ was estimated from equation (26), using the spectrum of the cross-stream velocity signal at the calibration point $(x/c, y/c) = (0.62, 0.022)$, a location which is slightly downstream of the reattachment point of the boundary layer. Figures 22a, 22b and 22c show the spectra at 3 locations at the suction side of the airfoil, at $x/c = 0.47, 0.53$ and 0.68 respectively. A very good agreement with the DNS spectra can be observed. On the other hand a significant discrepancy can be observed at the estimation of the spectrum in the wake, at $x/c = 2.0$, shown in Figure 22d.

This discrepancy reveals a pitfall of this model, which is related to the location of the

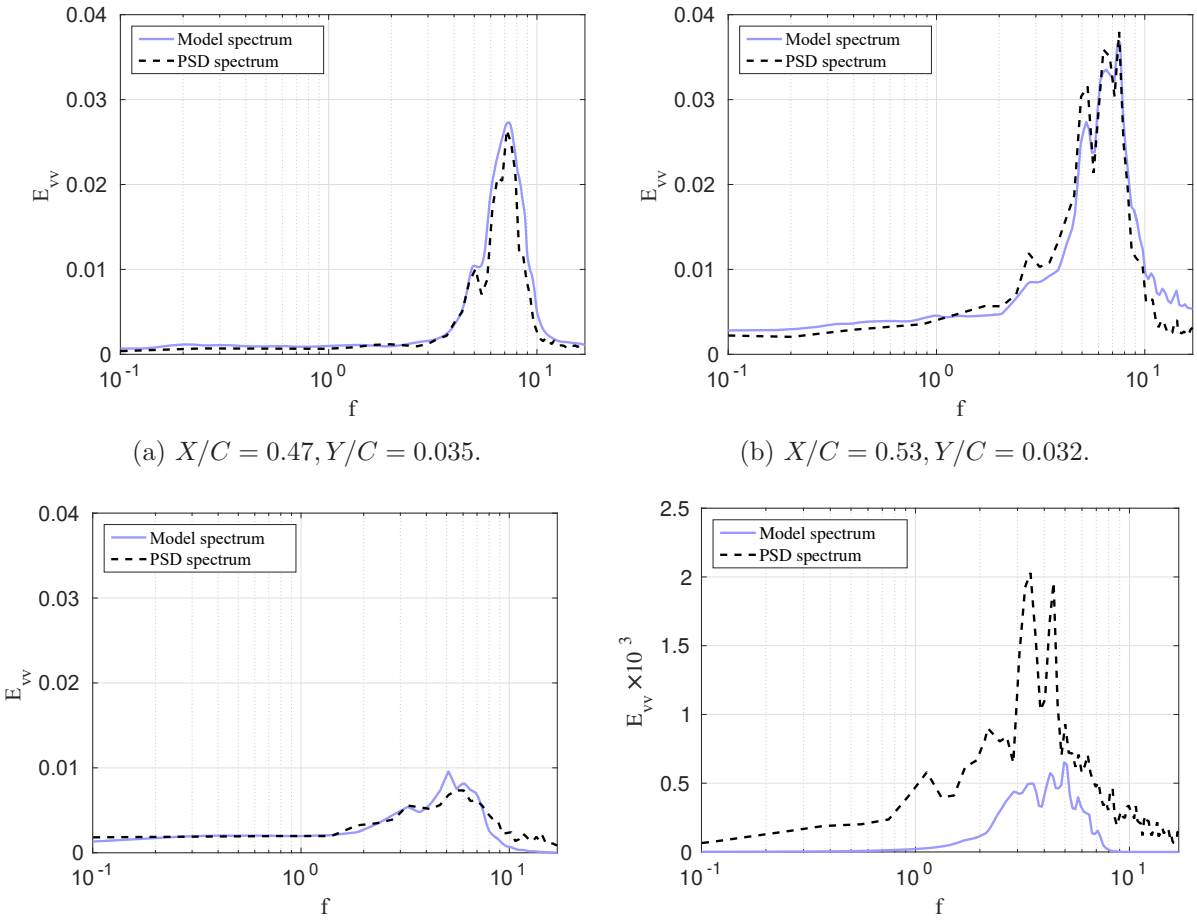

(a) $X/C = 0.47, Y/C = 0.035$.

(b) $X/C = 0.53, Y/C = 0.032$.

(c) $X/C = 0.68, Y/C = 0.012$.

(d) $X/C = 2.0, Y/C = -0.17$.

FIG. 22: Comparison between DNS and model spectra (calibration point $x/c = 0.62, y/c = 0.022$).

calibration point used to estimate $\Psi(\omega)$. If the point is located at a position in which the energy content of a specific frequency or range of frequencies is low, it is expected that the values of $\Psi(\omega)$ will not be calculated correctly at these frequencies. In a flow which is characterized by a single frequency (for example a bluff body wake as in the case studied by Gómez *et al.* [19]) this problem does not manifest itself, since the calibration point can be selected in an energetic area of the flow field, such as the wake. As it has been shown both in the current work and by [20], the flow field created by the straight trailing edge airfoil shows two dominant frequencies: the shear layer frequency, present on the suction side of the airfoil, and its sub-harmonic which develops further downstream in the wake. It is thus clear that if the calibration point used for calculating the weights $\Psi(\omega)$ is located on the suction side of the airfoil, at a point where the sub-harmonic frequency hasn't still fully developed, the values of $\Psi(\omega)$ at the corresponding frequencies will not be accurate.

This is exactly the case in the estimates shown in Figure 22, where the calibration point is located at $X/C = 0.62$, a point at which the dominant frequency is that of the shear layer. Consequently the values of $\Psi(\omega)$ at the nearby points $X/C = 0.47, 0.53$ and 0.68 are calculated correctly leading to the very good agreement seen in Figures 22a, 22b and 22c. The values, however, of $\Psi(\omega)$ at the smaller frequencies were erroneous, since the energy content of the spectrum at $X/C = 0.62$ at these frequencies is very small, leading to the very small values of the estimation shown in Figure 22d.

A solution to this problem, proposed by Beneddine *et al.* [11], is to use several points in the flow field (instead of a single point) and solve the, now over-determined, system of equations (26) (one equation for each point) in a least squares sense. If we select M points the minimization problem becomes:

$$\underset{\Psi(\omega)}{\text{minimize}} \quad \sum_{i=1}^{M} \|\hat{\boldsymbol{u}}(\boldsymbol{x}_i, \omega) - \Psi(\omega)\hat{\boldsymbol{u}}_1(\boldsymbol{x}_i, \omega)\|^2 \tag{27}$$

In Figure 23 the estimated spectrum is plotted again at the same streamwise location $x/c = 2.00$ in the wake. The difference is that the spectrum at an additional point located at $(x/c, y/c) = (1.40, -0.12)$ was also used to calculate the values of $\Psi(\omega)$ (the previous point at $X/C = 0.62$ was still used). As this figure reveals, using one more extra point in the wake has indeed corrected the discrepancy seen earlier in Figure 22d. The velocity signal at the second calibration point $x/c = 1.40$ has now enough energy in the frequency range of the wake to properly scale the values of the optimal response. The spectra estimates at the three other points were virtually unchanged and they are not plotted here.

The same method was applied for the blunt trailing edge airfoil; the results are shown in Figure 24 at the same locations as before. A single calibration point, located again at $(x/c, y/c) = (0.62, 0.022)$, was used to calculate $\Psi(\omega)$. A very good agreement can be observed at all points. The estimated spectra are very close to the actual ones, and the shedding frequency of $f_{bl,1} = 4.5$ is accurately predicted at all locations. The reason for the good agreement is the dominance of the shedding mode throughout the flow field in this case. Indeed, the flow is dominated by the Kárman shedding from the truncated trailing edge. The same frequency is also identified in the separating shear layer which is synchronised (locked) with Kárman shedding frequency. Thus the probing point at $X/C = 0.62$ contains enough energy at this frequency to correctly predict $\Psi(\omega)$ and, consequently, give accurate

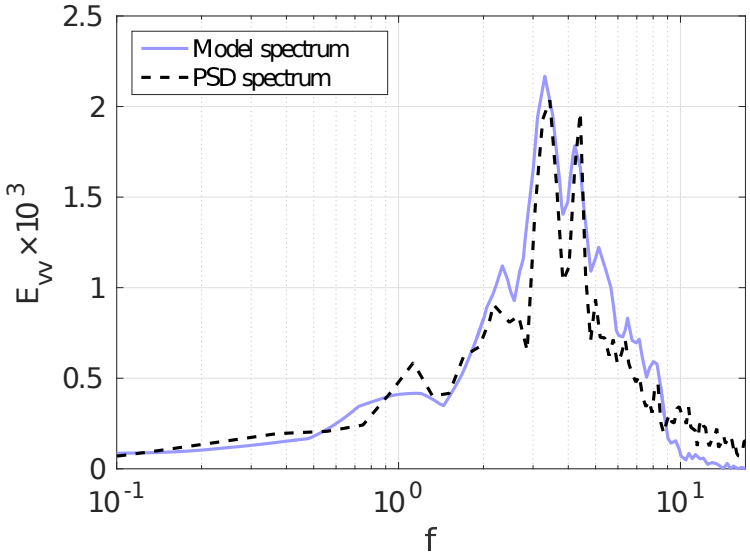

FIG. 23: Model spectrum at the wake point $(X/C = 2.0, Y/C = -0.17)$ using two calibration points to estimate $\Psi(\omega)$.

estimations for the entire spectrum.

We did not apply the spectra estimation to the tripped airfoil case for two reasons. Firstly, there is no clear separation of the two dominant singular modes, and secondly we have considered only two-dimensional perturbations ($k_z = 0$). While it is easy to account for the two neighbouring singular modes, the resolvent analysis for three-dimensional perturbations is more involved. In the naturally developing cases, the flow is dominated by the 2D Kelvin-Helmholtz instability and its subharmonic, so point measurements to compute the spectrum are justified. For the case of tripped airfoil though, the two dimensional component is weak due to the absence of recirculation. Therefore the instantaneous perturbation velocity must be first averaged in the spanwise direction to extract the $k_z = 0$ component and then Fourier transformed to obtain $\hat{\boldsymbol{u}}^{(i)}(\boldsymbol{x}_0, \omega)$; from this $\Psi(\omega)$ can be derived from (26). We did not store time-resolved velocity data at all points in the spanwise direction to be able to perform this operation. Furthermore, considering $k_z = 0$ components only, we cannot recover the spectra of the spanwise velocity in the z direction. For this, the system of equations (12) should be augmented to include the spanwise wavenumbers $k_z \neq 0$ (the relevant equations are well known, and can be found for example in [42]). The extraction of the singular values is now more time-consuming because a larger system must be solved at each frequency. The resolvent analysis must be applied for range of wavenumbers in the spanwise direction. We have not pursued this direction in the present paper, and we leave this as future work.

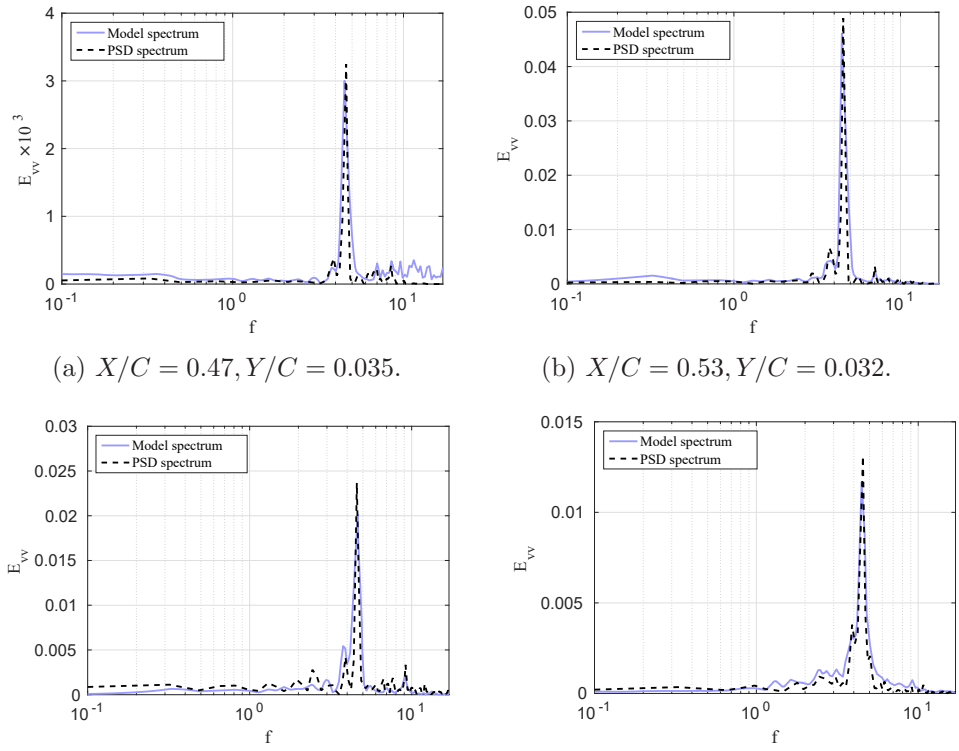

(a) $X/C = 0.47, Y/C = 0.035$. (b) $X/C = 0.53, Y/C = 0.032$.

(c) $X/C = 0.68, Y/C = 0.012$. (d) $X/C = 2.0, Y/C = -0.17$.

FIG. 24: PSD spectrum as calculated from the model (calibration at $X/C = 0.62, Y/C = 0.022$).

VI. Conclusions

In the present work, we studied the frequency response of separated and attached flows around a NACA-0012 airfoil. The resolvent operator was used that allows the study of the flow behavior from a systems point of view. It was assumed that the time-average flow is known, and the non-linear terms that appear in the transport equations for the flow perturbations around the mean were treated as a turbulent forcing term. For a given angular frequency ω, the resolvent operator provides a linear map between this forcing and the perturbations. A singular value decomposition of the resolvent provides the optimal forcings that will result in the maximum system response.

For the naturally developing flow around the standard NACA-0012 airfoil, the spectrum of the dominant singular value indicates very high amplification at the frequencies close to the natural frequency of the separated shear layer. The optimal forcing and response was also studied. It was revealed that the area most susceptible to forcing is the leading edge of the airfoil, up to approximately $x/c = 0.2$. The spatial structure of the forcing

was skewed against the mean flow, indicating that the Orr mechanism is responsible for the growth of perturbations upstream of separation. The spatial structure of the response was that of Kelvin-Helmholtz instabilities, which is known to develop in separating flows. The shape matched closely with the corresponding DMD mode obtained from processing the DNS results.

The resolvent operator was also applied to the naturally developing flow around a NACA-0012 airfoil with blunt trailing edge. For this case, the dominant singular value was reduced by almost an order of magnitude at the range of frequencies around the natural frequency of the separating shear layer found earlier. The resolvent spectrum was found to peak at the frequency of the Karman vortex shedding from the blunt trailing edge. Previous DNS simulations have demonstrated the lock-in of the separating shear layer to the shedding frequency, and the present resolvent analysis demonstrates the reduced receptivity of the separation bubble to forcing under lock-in conditions.

The third case examined was that of the tripped flow around the airfoil. Tripping suppressed the recirculation zone in a time-average sense, but resulted in distorted profiles that exhibited inflection points. The attached flow resulted in much smaller growth rates compared to the previous two cases (by almost two orders of magnitude) and the optimal response predicted by the resolvent analysis was present mainly in the wake. We repeated the resolvent analysis, computing the optimal response on a specific part of the domain around the suction side, and then we recovered the expected response at a frequency that matched the DNS results.

Finally, it was demonstrated how the resolvent analysis can be used to make accurate predictions of the spectra at any point in the flow field. For the straight trailing edge airfoil, two calibration points were needed. These must be located at regions where the fundamental and sub-harmonic Kelvin-Helmholtz modes have strong presence. For the blunt trailing edge airfoil, a single point was sufficient, because the flows in the suction side and the wake are locked to the vortex shedding, which is characterized by a single frequency. It has not been possible to predict the spectra for the tripped airfoil case, mainly because we have considered only two-dimensional perturbations ($k_z = 0$).

Acknowledgments

This work was funded by the MULTISOLVE project (Grant Agreement Number 317269) under the ITN Marie Curie framework of the European Commission. The simulations were performed in the Imperial College CX2 facility and in the UK HPC facility Archer (with access provided by the UK Turbulence Consortium, under grant EP/L000261/1).

---

[1] M Gaster, *On the stability of parallel flows and the behaviour of separation bubbles*, Ph.D. thesis, Queen Mary, University of London (1963).

[2] M Gaster, "Growth of disturbances in both space and time," The Physics of Fluids **11**, 723–727 (1968).

[3] PJ Schmid and DS Henningson, *Stability and transition in shear flows*, Vol. 142 (Springer Science & Business Media, 2012).

[4] JL Lumley, *Stochastic tools in turbulence*, 1st ed. (Elsevier, 1970).

[5] Lawrence Sirovich, "Turbulence and the dynamics of coherent structures. i. coherent structures," Quarterly of applied mathematics **45**, 561–571 (1987).

[6] PJ Schmid, "Dynamic mode decomposition of numerical and experimental data," Journal of Fluid Mechanics **656**, 5–28 (2010).

[7] BJ McKeon and AS Sharma, "A critical-layer framework for turbulent pipe flow," Journal of Fluid Mechanics **658**, 336–382 (2010).

[8] Tosio Kato, *Perturbation theory for linear operators*, Vol. 132 (Springer Science & Business Media, 2013).

[9] AS Sharma, I Mezić, and BJ McKeon, "Correspondence between Koopman mode decomposition, resolvent mode decomposition, and invariant solutions of the Navier-Stokes equations," Physical Review Fluids **1**, 032402 (2016).

[10] Rashad Moarref, Ati S Sharma, Joel A Tropp, and Beverley J McKeon, "Model-based scaling of the streamwise energy density in high-Reynolds-number turbulent channels," Journal of Fluid Mechanics **734**, 275–316 (2013).

[11] S Beneddine, D Sipp, A Arnault, J Dandois, and L Lesshafft, "Conditions for validity of mean flow stability analysis," Journal of Fluid Mechanics **798**, 485–504 (2016).

[12] D Sipp, O Marquet, P Meliga, and A Barbagallo, "Dynamics and control of global instabilities in open-flows: a linearized approach," Applied Mechanics Reviews **63**, 030801 (2010).

[13] Espen Åkervik, Uwe Ehrenstein, François Gallaire, and Dan S Henningson, "Global two-dimensional stability measures of the flat plate boundary-layer flow," European Journal of Mechanics-B/Fluids **27**, 501–513 (2008).

[14] F Alizard, S Cherubini, and JC Robinet, "Sensitivity and optimal forcing response in separated boundary layer flows," Physics of Fluids **21**, 064108 (2009).

[15] D Sipp and O Marquet, "Characterization of noise amplifiers with global singular modes: the case of the leading-edge flat-plate boundary layer," Theoretical and Computational Fluid Dynamics **27**, 617 (2013).

[16] A Monokroussos, E kervik, L. Brandt, and D.S. Henningson, "Global three-dimensional optimal disturbances in the Blasius boundary-layer flow using time-steppers," Journal of Fluid Mechanics **650**, 181–214 (2010).

[17] Fulvio Sartor, Clément Mettot, and Denis Sipp, "Stability, receptivity, and sensitivity analyses of buffeting transonic flow over a profile," AIAA Journal **53**, 1980–1993 (2014).

[18] F Gómez, HM Blackburn, M Rudman, AS Sharma, and BJ McKeon, "A reduced-order model of three-dimensional unsteady flow in a cavity based on the resolvent operator," Journal of Fluid Mechanics **798** (2016).

[19] F Gómez, AS Sharma, and HM Blackburn, "Estimation of unsteady aerodynamic forces using pointwise velocity data," Journal of Fluid Mechanics **804** (2016), 10.1017/jfm.2016.546.

[20] N Thomareis and G Papadakis, "Effect of trailing edge shape on the separated flow characteristics around an airfoil at low Reynolds number: A numerical study," Physics of Fluids **29**, 014101 (2017).

[21] S Balay, S Abhyankar, M Adams, J Brown, P Brune, K Buschelman, V Eijkhout, W Gropp, D Kaushik, M Knepley, *et al.*, *Petsc users manual revision 3.5*, Tech. Rep. (Technical report, Argonne National Laboratory (ANL), 2014).

[22] Robert D Falgout, Jim E Jones, and Ulrike Meier Yang, "The design and implementation of hypre, a library of parallel high performance preconditioners," in *Numerical solution of partial differential equations on parallel computers* (Springer, 2006) pp. 267–294.

[23] P Schlatter and R Örlü, "Turbulent boundary layers at moderate Reynolds numbers: inflow length and tripping effects," Journal of Fluid Mechanics **710**, 5–34 (2012).

[24] Stephen B Pope, *Turbulent flows* (Cambridge University Press, 2001).

[25] SM Hosseini, R Vinuesa, P Schlatter, A Hanifi, and DS Henningson, "Direct numerical simulation of the flow around a wing section at moderate Reynolds number," International Journal of Heat and Fluid Flow **61**, 117–128 (2016).

[26] PJ Schmid and L Brandt, "Analysis of fluid systems: Stability, receptivity, sensitivity. lecture notes from the flow-nordita summer school on advanced instability methods for complex flows, stockholm, sweden, 2013," Applied Mechanics Reviews **66**, 024803 (2014).

[27] L Lu and G Papadakis, "An iterative method for the computation of the response of linearised Navier–Stokes equations to harmonic forcing and application to forced cylinder wakes," International Journal for Numerical Methods in Fluids **74**, 794–817 (2014).

[28] Chih-Ming Ho and Patrick Huerre, "Perturbed free shear layers," Annual Review of Fluid Mechanics **16**, 365–422 (1984).

[29] F. Hecht, "New development in freefem++," J. Numer. Math. **20**, 251–265 (2012).

[30] Ian Jolliffe, *Principal component analysis* (Wiley Online Library, 2002).

[31] RB Lehoucq, DC Sorensen, and C Yang, *ARPACK users' guide: solution of large-scale eigenvalue problems with implicitly restarted Arnoldi methods* (SIAM, 1998).

[32] PR Amestoy, IS Duff, JY L'Excellent, and J Koster, "A fully asynchronous multifrontal solver using distributed dynamic scheduling," SIAM Journal on Matrix Analysis and Applications **23**, 15–41 (2001).

[33] Xavier Garnaud, Lutz Lesshafft, PJ Schmid, and Patrick Huerre, "The preferred mode of incompressible jets: linear frequency response analysis," Journal of Fluid Mechanics **716**, 189–202 (2013).

[34] LE Jones, RD Sandberg, and ND Sandham, "Stability and receptivity characteristics of a laminar separation bubble on an aerofoil," Journal of Fluid Mechanics **648**, 257–296 (2010).

[35] G Desquesnes, M Terracol, and P Sagaut, "Numerical investigation of the tone noise mechanism over laminar airfoils," Journal of Fluid Mechanics **591**, 155–182 (2007).

[36] D Rodriguez and V Theofilis, "Structural changes of laminar separation bubbles induced by global linear instability," Journal of Fluid Mechanics **655**, 280–305 (2010).

[37] Kathryn M Butler and Brian F Farrell, "Three-dimensional optimal perturbations in viscous shear flow," Physics of Fluids A: Fluid Dynamics **4**, 1637–1650 (1992).

[38] AV Dovgal, VV Kozlov, and A Michalke, "Laminar boundary layer separation: instability

and associated phenomena," Progress in Aerospace Sciences **30**, 61–94 (1994).

[39] PJ Strykowski and DL Niccum, "The influence of velocity and density ratio on the dynamics of spatially developing mixing layers," Physics of Fluids A: Fluid Dynamics **4**, 770–781 (1992).

[40] LE Jones, *Numerical studies of the flow around an airfoil at low Reynolds number*, Ph.D. thesis, University of Southampton (2008).

[41] S Beneddine, R Yegavian, D Sipp, and B Leclaire, "Unsteady flow dynamics reconstruction from mean and point sensors: an experimental study," Journal of Fluid Mechanics **824**, 174–201 (2017).

[42] W Zhang and R Samtaney, "Biglobal linear stability analysis on low-re flow past an airfoil at high angle of attack," Physics of Fluids **28**, 044105 (2016).